# Equivalent Magnetic Network Modeling of Variable-Reluctance Fractional-Slot V-Shaped Vernier Permanent Magnet Machine Based on Numerical Conformal Mapping

Mehrage Ghods, Jawad Faiz, *Senior Member, IEEE*, Hamed Gorginpour, Mohammad Amin Bazrafshan, Jonas Kristiansen Nøland, *Senior Member, IEEE*

*Abstract*-- The V-shaped permanent magnet synchronous machine (PMSM) has been successfully commercialized in hybrid- and all-electric vehicles fabricated by several famous companies. The advantages of PMSMs are a wide constant torque-speed range, high torque development capability and high power factor, and low torque ripple. In addition, the Vernier-PM (VPM) machines supersede conventional PMSM's torque density and cogging torque. This paper presents a variable-reluctance fractional-slot V-shaped VPM (VR-FS-VVPM) machine with special rotor core surface. Hence, varying the air gap length over the direct and quadrature axes decreases the torque ripple considerably. Moreover, design of the PM-housing differs from previously introduced V-shaped VPM structures. As a result, the leakage flux in the yoke-side end-portion of the PM pieces reduces, enhancing the flux-linkage and power factor. To facilitate the design process further, an innovative equivalent magnetic network (EMN) model is established to improve performance prediction analytically. Moreover, conformal mapping is applied to create the permeance network for complex geometry air gap region. Here, a pentagonal-shape mesh-cell is used in the air gap region for capturing flux behaviour more accurately. The introduced method predicts the performance of the proposed VR-FS-VVPM machine. Finally, a typical 500 W, 12-slot/16-pole motor is designed and prototyped to validate the EMN-modelling against finite element analysis and experimental results.

*Index Terms*-- Vernier-PM machine, numerical mapping, equivalent magnetic network model, magnetic equivalent circuit.

## I. INTRODUCTION

NOWADATDS, the Vernier-PM (VPM) machine, which combines the magnetic gear effect into PM synchronous machine (PMSM), has gained considerable interest. The reasons include high torque density capability and appropriate operating features over a wide range of speeds. Therefore, it is considered a good option for applications such as wave and wind generators, ship propulsion motors, and in-wheel motors

M. Ghods, J. Faiz and M. A. Bazrafshan are with School of Electrical and Computer Engineering, College of Engineering, University of Tehran, Iran.

H. Gorginpour is with Engineering Department of Engineering, Persian Gulf University, Bushehr, Iran

J. K. Nøland, is with Department of Electric Power Engineering, Faculty of Information Technology and Electrical Engineering, NTNU, Norway.
.

proposed for VPM machines, including radial, axial, and linear flux topologies [1-3]. Radial-flux VPM machines are the most common topology. Examples are surface-mounted, consequent-pole, and alternating flux barrier topologies. Others include dual-stator spoke array VPM machine, schemes with stator PM inserted in the slot opening, in the split-tooth, and in the tooth, while PMs can be also mounted on the tooth surface [4-7].

V-shaped interior PM machines are known for their widespread constant torque-speed region and enhanced operation including high efficiency, improved power factor, and low torque ripple. An inner rotor V-shaped VPM machine is proposed in [8], and the operating quantities of its optimum designed structure are compared with those of conventional V-shaped PMSM. Here, it is found that the VPM machine can achieve a much higher torque/volume ratio with considerably lower torque ripple and comparable efficiency. The cogging torque of the optimally designed motor is 7.3 %. Alternatively, an outer rotor V-shaped VPM motor is presented in [9]. It has superior performance in developing higher average torque with lower cogging torque compared with an outer rotor spoke-type VPM motor. Each stator tooth creates two flux modulation poles, and there are dummy slots on the inner surface of the rotor core. It is shown that high-speed harmonics in the air gap flux density and low-speed harmonics with high amplitude can be fully utilized. In addition, the flux leakage can be avoided effectively by utilizing the proposed V-shaped PM topology in the rotor. These advantages are only achieved through finite element analysis (FEA); clearly, the power factor of VPM machines considerably decreases by the presence of flux modulation poles, its power factor has not been reported. In both V-shaped VPM topologies presented in [8] and [9], there are narrow width regions in the rotor core leading to high flux density and leakage flux, thus, reducing the power factor.

This paper presents the design and modeling of a high-torque-density variable reluctance fractional-slot V-shaped VPM (VR-FS-VVPM) machine for a mid-drive e-bike application. The special sinusoidal shape of the rotor core peripheral leads to a very low cogging torque. However, the special rotor design makes the flux routes more complicated,

This article has been accepted for publication in IEEE Transactions on Transportation Electrification. This is the author's version which has not been fully edited and content may change prior to final publication. Citation information: DOI 10.1109/TTE.2023.3235333

2

and therefore, it requires an accurate analytical model to predict the performance for parametric design optimization purposes. Here, the flux routes through the air gap region are essential for capturing the machine operating characteristics. Moreover, flux barriers exist in the design of the PM insertion housing to decrease the leakage flux in the yoke-side end-portion of the PM segments. Although this PM housing design differs from the previously introduced V-shaped VPM structures, it is used for V-shaped interior PM (IPM)-PMSM with asymmetrical PM pieces placed in two halves of V-shaped housing [10]. Such design is more important in the case of VPM machines considering their higher flux leakage and lower power factor.

An analytical model with reasonable accuracy is essential for a thorough parametric analysis at the design stage of electrical machines. To solve the voltage equations, winding function theory with Fourier transformation is often used for the analytical modeling of VPM machines [11]. In the application of the winding function method, the magnetization characteristic of the ferromagnetic core is assumed linear. The FEA model considers complex details of the machine precisely, including slot effects, non-linearity of magnetization characteristic of the iron core, and core losses. Generally, the analytical models results are validated by comparing them with that of FEA. However, the computational burden of FEA is very high, and simultaneous altering some geometrical dimensions, winding layout, and the number of PM pieces is impossible. Therefore, analytical modeling approaches, such as magnetic equivalent circuit (MEC) and layer models, are developed to deal with these inherent design challenges.

In recent years, analytical models such as sub-domain, flux-tube, and MEC have gained considerable interest in electrical machine design and optimization. The MEC model can even consider the non-linear properties of the iron core and model the magnetic flux lines in different parts, especially in the air gap region, with reasonable accuracy. Besides, slot skew can be taken into account using the concept of quasi-3D MEC modeling. Moreover, the MEC model can predict the magnetic field distribution, and estimate the core losses, even including the optimal design of linear PMSM [12]. The performance of a PM machine with surface-mounted and Halbach PM arrays has been analyzed using MEC models [13, 14]. In addition, a MEC model for a switched reluctance motor has been presented with a special rotor structure that can precisely model the non-linear characteristic, magnetic saturation, and flux leakage in a time-efficient solving algorithm [15]. The modeling approach has also been shown to predict both the no-load and on-load performance of the machine [16]. The magnetic permeances in MEC modeling is based on the overall behavior of the flux lines in each region, and the exact details of all flux routes are omitted. Besides, the leakage flux lines are often neglected for the sake of simplicity.

The reluctance network model (RNM) has been introduced in [17] to overcome the weaknesses of the conventional MEC method, especially in the case of PM machines with considerable leakage flux and complex flux routes. An arbitrary number of fined meshes can be placed in some regions to model the complex flux behavior. The equivalent magnetic-network (EMN) has been proposed in [18] by combining RNM and MEC modeling methods. The meshed networks have been created for modeling complex flux routes in regions such as air gap and pole shoes, and the other sections of machine structure such as tooth bodies and yokes are simply modeled based on the MEC method. Higher accuracy compared to the other analytical models and shorter computational time in comparison to FEA are the advantages of the EMN model. Since the resulting system of equations comprises non-linear elements, iterative methods such as Newton-Raphson, Gauss-Seidel, and SOR methods should be used to establish a recursive solving algorithm.

VPM machines have flux lines with complex behavior and large leakage flux compared to conventional electric machines, therefore, in this paper the EMN model is established to analyze the proposed VR-FS-VPM machine. The conformal mapping [19] is applied to simplify the complex geometry of the air gap region. To rearrange the mesh networks which change with the rotor position, the continuous positioning method is used. In this way, the spikes superimposed on the post-processing waveforms due to numerical errors are diminished in comparison to the discrete positioning method. In addition, by using the continuous positioning method the number of mesh layers and, thus, the computing time shortens with negligible impact on the accuracy. To define the flux tubes in the air gap region, a special pentagonal shape mesh is selected which is capable of capturing the flux routes. Besides, for modeling the regions between the PM pieces including flux barriers, the air gap region, mesh networks are used. The resulted analytical system of equations, considering the exact magnetization characteristic of the magnetic core, is solved using the recursive Gaussian elimination method.

The novelties and new contributions of this paper include:
* A fractional-slot V-shaped VPM machine with sinusoidal variable air-gap length is proposed aiming to reduce the cogging torque.
* Since Vernier machine is a flux modulation machine, it has irregular flux lines in stator and rotor cores near the air gap and in the air gap region itself. In addition, its flux lines comprise flux leakage and fringing routes. Hence, to improve the accuracy of the model in the proposed modeling approach the following items are considered:
  ✓ Stator poles shoes uses permeance network.
  ✓ A mesh network is applied for rotor core regions inside the V-shaped PM housings, which has not been reported previously.
  ✓ The air gap region is modeled by pentagonal mesh cells, to consider all possible flux routes in radial and axial directions. It is noted that there is a compromise between the reasonable accuracy and short computation time in choosing the number of meshing layers.
  ✓ EMN method can easily model the curved shape flux lines, taking into account the effects of slotting,

skewing, fringing flux, leakage flux in slots, core saturation, , and stator and rotor doubly-saliency. These are too difficult or impossible to be considered in winding function and traditional MEC modeling techniques.

✓ A conformal mapping method is used to convert variable reluctance air gap to an air gap with constant length and the relations between original and mapped quantities is extracted.

✓ The continues positioning method in proposed EMN method is another important advantage compared to the MEC method. This method, which is based on the defining variable permeances for connecting air gap nodes with stator boundary ones, yields very significant reduction of numerical spikes in the output characteristics waveforms.

The paper is organized as follows: Section II presents the structure of the proposed fractional-slot variable reluctance V-shaped VPM machine. The effects of designing PM housing with no iron bridge in yoke-side end-portion and sinusoidal shaping of rotor core peripheral on the operating quantities are investigated. Section III introduces the EMN model of the structure with comprehensive details of creation of magnetic networks modeling of each machine part and calculation of the network permeances. Section IV discusses the conformal mapping method application for converting the complex geometry air gap region to a simplified geometrical shape. Section V presents the continuous positioning method for defining the variable permeances connecting mesh networks of rotor core to the boundary layer of pentagonal shape mesh cells of air gap region. Section VI presents the non-linear time stepping solving algorithm based on Gaussian-elimination recursive method; the accuracy and effectiveness of the analytical model is studied by comparing its results and solution time with those of FE method and experimental results.

## II. STRUCTURE OF PROPOSED VR-VPM MACHINE

The operating principle of VPM machine is based on the flux modulation of rotor magnets with variable air gap reluctance due to stator poles. The magnetic gear ratio ($G_r$) is obtained as follows:

$$P_s = N_{FMP} \pm P_r \quad \Rightarrow \quad G_r = -\frac{\omega_s}{\omega_r} = -\frac{P_r}{P_s} \qquad (1)$$

where $P_s$ and $P_r$ are the stator and rotor pole pair numbers, respectively, and NFPM is the number of stator modulation pole.

The developed electromagnetic torque of surface-mounted structure is almost synchronous torque and its reluctance torque component is negligible. However, there is reluctance torque component in interior-PM type VPM machine, which results in a higher cogging torque. The spoke-array and V-shaped arrangements of rotor PMs are common types of IPM machines.

The outer-rotor V-shaped VPM machine is compared with outer-rotor spoke-type VPM machine in [8] and it is revealed

that V-shaped structure has higher average torque and considerably lower torque ripple. Vernier motors have lower cogging torque compared with the conventional PM motors. Among different PMs arrangements, the V-shaped structure has even lower cogging torque. In this paper, the aim is to reduce the cogging torque compared with the previous designs.

The interaction between PM magnetic field and the stator teeth creates the cogging torque. The cogging torque is higher in IPM machines than that of the surface mounted machines, because of its shorter air-gap length. Increasing the average air-gap length can attenuate this oscillating torque. However, this yields to diminish average torque, which is not desirable. In the proposed design, the attraction between PM field and stator teeth decreases by increasing the air-gap length in q-axis direction in sinusoidal shape variations. In addition, the reluctance torque with high pulsation nature is developed in IPM machines due to difference between d- and q-axes inductances, which results from unequal d- and q-axes equivalent reluctances. This difference can be decreased by sinusoidal variation of the air-gap length with placing the



$$g_{var}(\theta_m, \varphi) = \frac{g_{max} + g_{min}}{2} + \frac{g_{max} - g_{min}}{2} sin(2P_r.(\theta_m - \varphi))$$
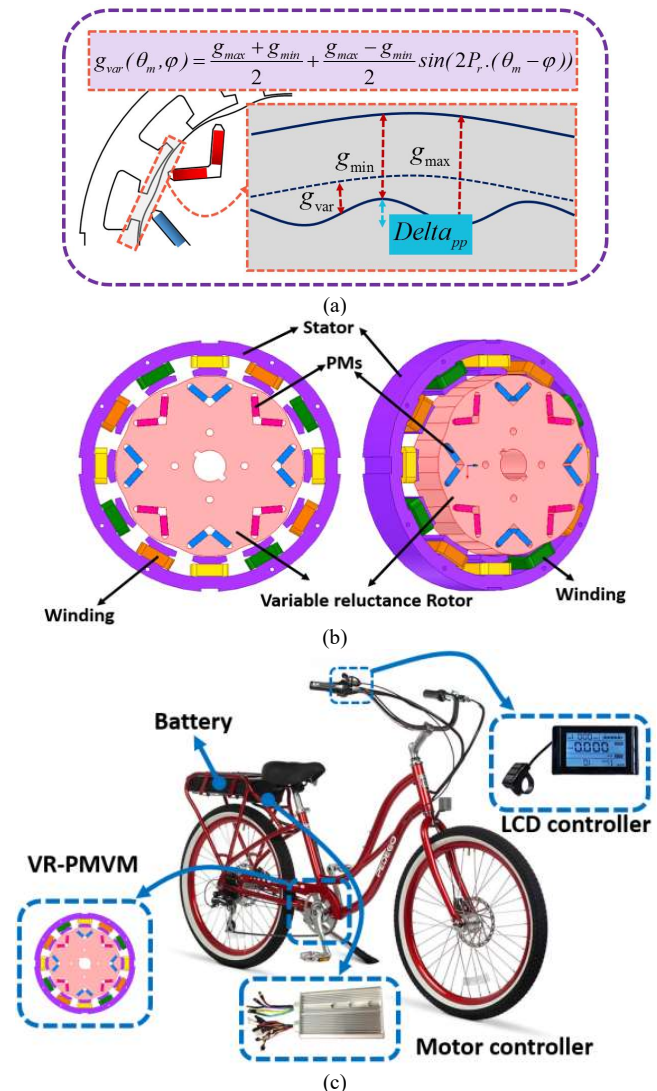
(a)

(b)

(c)

Fig. 1. (a) Sinusoidal shaping of rotor core peripheral and variable air gap length, (b) 2D and 3D cross sections of the proposed VR-VVPM motor, (c) in-wheel motor application.
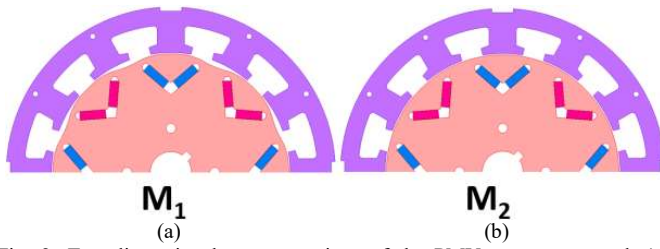
Fig. 2. Two-dimensional cross sections of the PMV motor proposed, (a) variable air gap ($M_1$), (b) uniform air gap ($M_2$).

maximum length in q-axis and minimum length in d-axis directions, as shown in Fig. 1 (a)

Therefore, a sinusoidal-shape structure for the rotor core outer surface has been suggested, and its capability in the cogging torque reduction has been proved. Fig. 1(b) shows the structure of the proposed variable-reluctance V-shaped VPM machine. This three-phase inner-rotor machine is used in a mid-drive e-bike as shown in Fig. 1(c). Several design optimizations have indicated that the operating quantities are improved using variable reluctance rotor core ($M_1$ design in Fig. 2(a)) instead of a conventional round rotor core ($M_2$ design in Fig. 2(b)). There are 12 concentrated coils on the stator core, as such that their conductors are inserted side by side in the stator slots leading to an 8-pole fractional-slot winding.

The optimum saliency ratio of air gap length variation can be obtained by sensitivity analyses. Fig. 3 depicts the curves of average and cogging torque, efficiency and output power versus peak-to-peak air gap length. The proposed EMN model, presented in Section III, is used for these studies.

According to the results, the peak-to-peak value of 0.6 mm is selected as the optimum value in this paper and fabricating the prototyped machine. Based on the previous PM housing designs on V-shaped VPM machine [4, 8], the leakage flux at the end of the PM segment increases, which reduces the efficiency and power factor and causes local saturation in the iron bridge between the two halves of the housing. A different design is used here for PMs housing, leading to less leakage flux in the yoke-side housing end; these flux lines are aligned with the main flux, which improves the efficiency and power factor and prevents the local saturation. Table I lists the

TABLE I
GEOMETRICAL DIMENSIONS AND SPECIFICATIONS OF THE
STUDIED VR-FS-VPM MACHINE

| Parameter | Value |
|---|---|
| Speed (rpm) | 1200 |
| No. of stator pole pairs ($P_s$) | 8 |
| No. of flux modulating poles ($N_{FMP}$) | 12 |
| No. of rotor pole pairs ($P_r$) | 4 |
| Stator turns per coil | 20 |
| Stack length (mm) | 25 |
| PM thickness (mm) | 3 |
| PM width and length (mm×mm) | 10×25 |
| Stator inner/outer diameter (mm) | 87/120 |
| Rotor inner/outer diameter (mm) | 25/86 |
| Slot opening width (mm) | 8 |
| Air gap length (mm) | 0.5 |
| Rated power (W) | 450 |
| Rated current (A) | 14 |
| Remanence of PM, $B_{rem}$ (T) | 1.32 |
| PM material (NdFeB) | N42-SH |
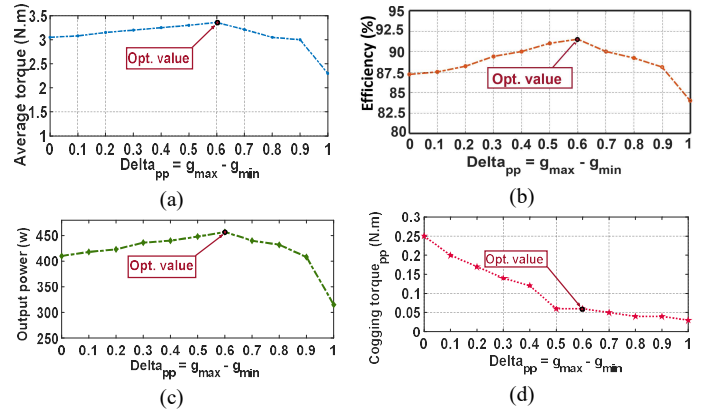


Fig. 3. Sensitivity analyses for finding optimum value of air gap length variation, (a) average electromagnetic torque, (b) efficiency, (c) output-power, and (d) cogging torque.

specifications of the designed VR-FS-VVPM machine.

The two-dimensional (2D) FEA results for $M_1$ and $M_2$ designs with the same specifications are compared. As shown in Fig.4, the torque ripple in the $M_1$ design with variable air gap length is much lower than that of the $M_2$ design. In addition, the power factor and efficiency of the $M_1$ design are improved, and its back-electro-motive force (EMF) waveform is sinusoidal and smoother.

As shown in Fig. 5(a), iron bridges in yoke side end-portion of the PM housings of V-shaped VPM machine was previously used. These bridges cause local saturation and increase leakage flux. The yoke side bridge of PM housing is removed in the proposed structure. Fig. 5(b) shows the modified design of PM housing. Hence, another modification is the design of V-shaped housing for inserting PM pieces. There is no iron bridge between the two halves of the PM housing, which desirably acts as a flux barrier to the flux leakage lines in the end-portion of the PM pieces. Therefore, as illustrated in Fig. 5(c), the flux leakage lines force to contribute as main flux lines and enhance the power factor and output power,

The proposed structure here consists of 4 PM pole-pairs on the rotor core and 12 stator teeth. According to the general relationship for flux modulation, the stator winding can be wound with 8 or 4 pole-pairs. The selected number of pole-pairs is 4 considering the negative sign in (1).
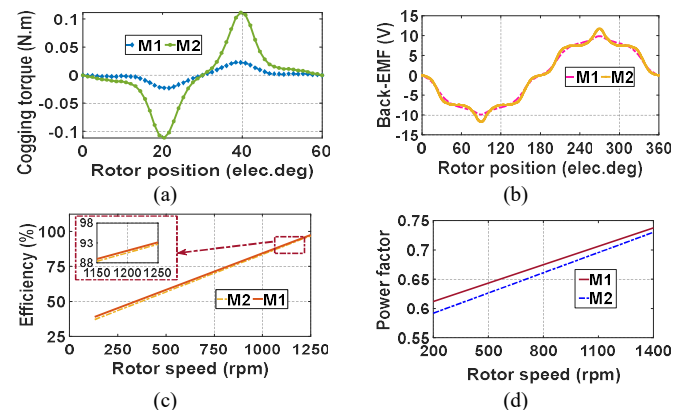


Fig. 4. Comparison of FEA results, (a) cogging torque, (b) back-EMF, (c) efficiency, and (d) power-factor.
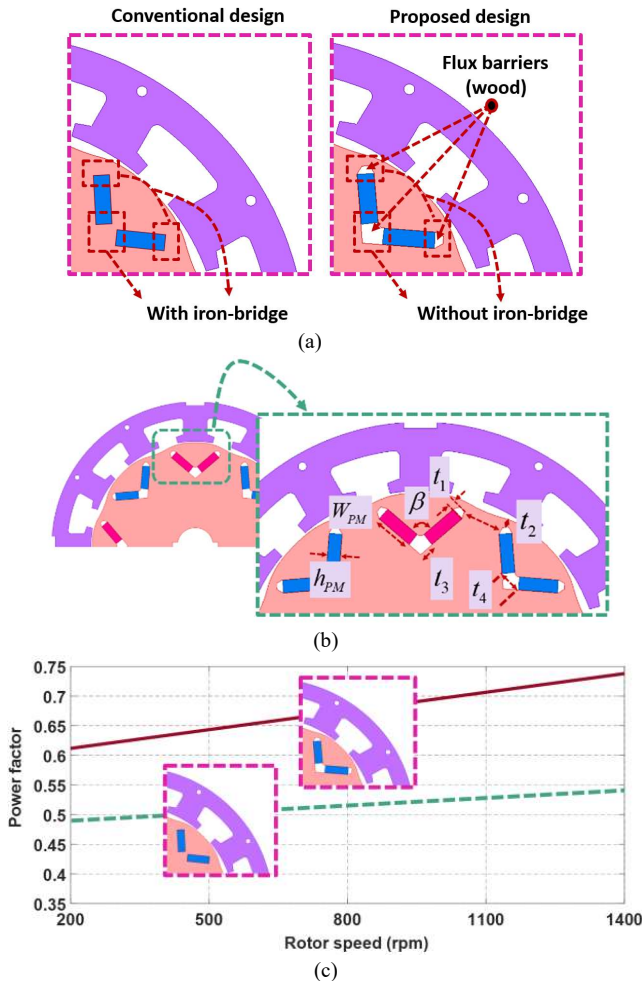
Fig. 5. (a) V-shaped arrangement with and without iron-bridge in yoke-side end-portion of PM housing, (b) modified PM housing for presented VR-FS-VVPM machine, (c) comparing the power factor curves of $M_1$ design machine with Modified and conventional V-shaped PM housing structure.

Fig. 6(a) depicts the winding layout of a three-phase, 12 slots, 4 pole-pairs fractional slot winding. Fig. 6(b) shows the spatial harmonic components of the stator winding magnetic field. As seen, 4 and 8 pole-pairs are the dominant components of the stator magnetic field. Besides, a PMSM can be created by coupling 4 pole-pairs component of stator field and PM field under the appropriate excitation frequency. In addition, a VPM machine can be introduced by coupling the modulated field of PMs through air gap permeance and 8 pole-pairs component of stator field. The back-EMF and torque equations of a VPM machine consist of two terms. The first term is identical with that of the conventional PM motor and the second term increases the induced EMF and developed torque.

Fig. 6(c) shows the torque-speed characteristics of the proposed machine when driving as a conventional PMSM and VPM machines which have been obtained using FEA at the rated operating speed. As shown, the excitation frequencies are different in the case of PMSM and VPM machine.

The EMN model of the $M_1$ structure is presented in the next section. It should be noted that the proposed structure and developed model can be applied in the case of VPM structures with different gear ratios without lack of generality.
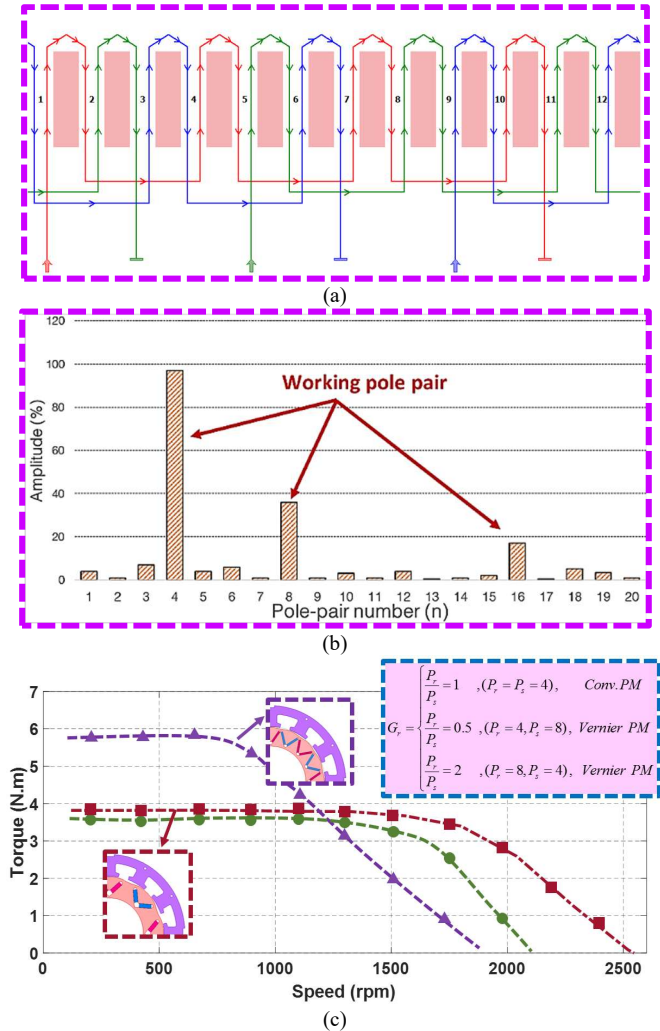


Fig. 6. (a) Winding layout of a 12 slots/8 pole-pairs fractional-slot winding, (b) spatial harmonic components of winding function of a 12 slots/8 pole-pairs fractional-slot winding, (c) comparison between torque-speed characteristics of a 4 pole-pairs conventional PMSM and a VPM machine with 4 PM pole-pairs and 8 stator winding pole-pairs.

## III. EQUIVALENT MAGNETIC NETWORK M MODEL

The MEC model in an electric machine is the series connection of magnetic reluctances and a MMF sources. The system of equations is obtained from the resulted magnetic circuit by writing Kirchhoff voltage law (KVL) and Kirchhoff current law (KCL) equations. The number of flux tubes can be increased in a region with complex flux routes or where a higher accuracy is required. The meshed network with higher resolution results in a higher precision at the cost of higher computational burden. There are several routes for passing flux lines from tooth tip into the air gap. The magnetic flux passing from each network section is calculated by multiplying the magnetic permeance of that section and magnetic potential difference between end points of the route. The magnetic potential of nodes are unknown values.

The placement of flux tubes and defining their related permeances in the EMN model are based on the magnetic flux lines obtained by FEA. The EMN model introduces an effective analytical method with a higher precision than the other analytical modeling approaches and the computational burden
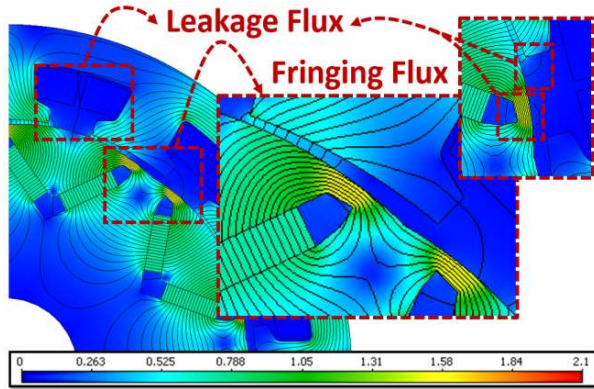
Fig. 7. 2D flux pattern of the proposed VPM machine in the air gap region, fringing and leakage flux lines.

lower than the FEA. While, a mesh network is considered for regions with complex flux lines routes, the regions with regular flux routes are modeled with lumped permeances similar to MEC method. At the beginning of the modeling procedure, the FEA is required to detect the flux behavior in different regions. For example, to consider the leakage and fringing fluxes and irregular flux routes due to saturation effects, mesh networks model the pole shoe and slot opening regions of stator core and only one lumped permeance is required for each of these regions. In this way, the number of mesh nodes and the dimensions of the matrices in numerical solving algorithm remain limited and the accuracy is not deteriorated. There is no need to perform FEA in the next steps and no parameter or other required data are extracted from FEA results. In addition, the categories of regular or irregular flux regions are not modified with variations in the specifications of the proposed machine. Fig. 7 presents the regular flux routes for stator yoke, teeth and rotor yoke of $M_1$ design. However, magnetic saturation, leakage and fringing flux, magnetic field modulation and complex routes of flux in the air gap, stator tooth tips and PM housing regions make it difficult to apply MECs. Hence, meshed networks with higher number of nodes should be considered in these regions for accurate capturing of flux lines behavior.

### A. Calculation of MMF sources and permeances in stator region

Fig. 8 depicts the permeance network modeling of different parts of the stator region. This network is similar to the network presented in [11]. However, the leakage flux inside the slot is modeled by three permeances instead of one permeance with the advantage of achieving a higher accuracy under on-load operating. The MMF sources in this network are calculated as follows:

$$F_{ad} = F_{au} = N_c i \tag{2}$$

where $N_c$ is the number of conductors in each stator coil and $i$ is the phase winding current. The stator region of VR-FS-VPM machine can be divided into three parts including yoke, tooth body and tooth tip or modulators. The permeances of each yoke section ($P_{ys}$), a tooth body ($P_t$) and the network placed in
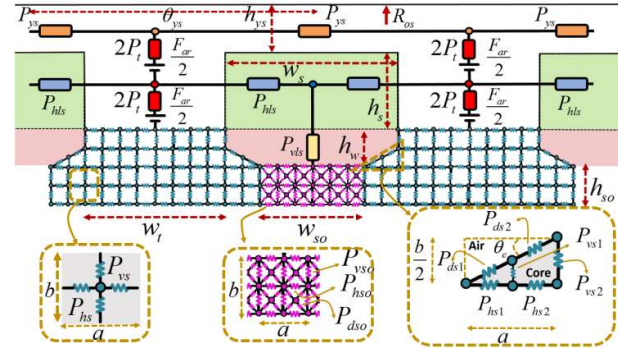


Fig. 8. Constant permeance of the stator.

each tooth shoe are derived as follows:

$$P_{ys} = \mu_c L_{stk} \frac{h_{ys}}{W_t + W_s} \quad , \quad P_t = \mu_c L_{stk} \frac{W_t}{h_s} \tag{3}$$

In Fig. 8, the slot area is divided into conductor section, air section and slot opening section. In slot opening section, a mesh network with vertical and horizontal permeances are placed for more realistic capture of the flux lines. The equivalent permeances modeling conductor and air sections are calculated as follows:

$$P_{hls} = \mu_o L_{stk} \int_0^{h_s} \left( \frac{A_{coil}}{A_{slot}} \right)^2 \frac{dx}{y} = \frac{2}{3} \mu_o L_{stk} \left( \frac{h_s}{W_s} \right) \tag{4}$$

$$P_{vls} = \frac{P_{vls1} \cdot P_{vls2}}{P_{vls1} + P_{vls2}} \quad \rightarrow P_{vls1} = \mu_o L_{stk} \frac{W_s}{h_w / 2}$$

$$and \quad P_{vls2} = \mu_o L_{stk} \frac{1}{\dfrac{1}{2} \displaystyle\int_0^{h_w/2} \dfrac{dy}{\dfrac{W_s}{2} - \dfrac{W_s - W_{so}}{h_w} y}}$$

$$= 2\mu_o L_{stk} \frac{W_s - W_{so}}{h_w} \times \frac{1}{Ln \dfrac{W_s}{W_{so}}} \tag{5}$$

where $A_{coil}$ is the effective area occupied with the conductors and $A_{slot}$ is the slot area. It is noted that the vertically placed permeance $P_{vls}$ consists of two components placed in the conductor and air regions with series connection.

A mesh network should be placed in tooth tip region due to the irregular flux lines routes in this region. The horizontal $P_{hs}$ and vertical $P_{vs}$ permeances of each square shaped mesh are evaluated as follows:

$$P_{hs} = \mu_c L_{stk} \frac{b}{\displaystyle\int_{-a/2}^0 dx} = \mu_c l_{stk} \frac{2b}{a} \quad , \quad P_{vs} = \mu_c L_{stk} \frac{2a}{b} \tag{6}$$

The analytical equations for calculating permeances of triangular shape meshes in tooth tip network are given in (6)-(10). Fig. 8 shows these permeances and they are as follows:.

$$P_{vs2} = \mu_c L_{stk} \frac{1}{\displaystyle\int_0^{a/4} \dfrac{dx}{\dfrac{b}{2} + \dfrac{2b}{a} x} + \int_{a/4}^{a/2} \dfrac{dx}{b}} \approx 1.67 \mu_c L_{stk} \frac{b}{a} \tag{7}$$

$$P_{hs2} = \mu_c L_{stk} \frac{1}{\int_0^{b/2} \frac{dy}{a - \frac{a}{2b}y}} \approx 1.74 \mu_c L_{stk} \frac{a}{b} \tag{8}$$

$$P_{hs1} = \mu_c L_{stk} \frac{1}{\int_{a/2}^a \frac{dy}{b - \frac{b}{2a}y}} \approx 1.23 \mu_c L_{stk} \frac{b}{a} \tag{9}$$

To solve the problem of infinite permeance due to zero area in sharp points, the triangular shape mesh in $P_{vs1}$ calculation is approximated as a rectangular shape with the same area:

$$P_{vs1} = \mu_c L_{stk} \frac{1}{\int_{a/4}^{a/2} \frac{dx}{\frac{2a}{b}x}} = \mu_c L_{stk} \frac{2}{Ln2} \frac{a}{b} \approx 2.9 \mu_c L_{stk} \frac{a}{b} \tag{10}$$

In addition, for boundary permeances ($P_{ds1}$ and $P_{ds2}$) calculation, the mesh area is rotated with $\theta_e$ angle to solve the problem of integration bounds. In this way, the mesh shape is considered as an equivalent rectangular one:

$$P_{ds1} = P_{ds2} = \mu_c L_{stk} \frac{b/4}{\frac{a/2}{\cos\theta_e}} = \frac{1}{2}\mu_c L_{stk} \frac{b}{\sqrt{a^2 + \left(\frac{b}{2}\right)^2}} \tag{11}$$

The permeances of slot opening network are as follows:

$$P_{hso} = \mu_o L_{stk} \frac{2b}{a} \ , \ P_{vso} = \mu_o L_{stk} \frac{2a}{b} \ ,$$
$$P_{dso} = \mu_o L_{stk} \frac{b}{\sqrt{b^2 + a^2}} \tag{12}$$

It is worthy to note that diagonal permeances are considered for this mesh network to better capturing the leakage flux routes in this region and enhancing the modeling accuracy. For the sake of simplicity, the dimensions of all mesh cells are considered the same for omitting different values of the permeances.

### B. Calculation of PM MMF Sources and Permeances in Rotor Region

Fig. 9(a) shows the schematic overall view of stator and rotor permeances. Fig. 9(b) illustrates the notations used for rotor network permeances and their relations are given by (14)-(21). The magnetic characteristics of PM material, i.e. NdFeB magnet type N42-SH, is considered linear with constant magnetic permeability. The magnet pieces are of bar shape and can be modeled as a series connection of MMF source and a permeance:

$$F_{PM} = H_{PM} h_{PM} = \frac{B_{rem} h_{PM}}{\mu_{PM}} \ ,$$
$$P_{PM} = \mu_{PM} \frac{W_{PM} L_{stk}}{h_{PM}} \ \rightarrow \ P_{PM2} = 2P_{PM1} = \frac{2}{3}P_{PM} \tag{13}$$

According to Fig. 9(b), the magnetic permeance of a PM piece is divided into two permeances denominated with $P_{PM1}$ and $P_{PM2}$ covering 1/3 and 2/3 of magnet length, respectively. This is due to denser flux lines in the end portion of PM segment:

$$P_{ry} = \mu_c \frac{l_{stk}}{\theta_{ry}} \ln \frac{R_{ry2}}{R_{ry1}} \tag{14}$$

$$P_{rv1} = \mu_c L_{stk} \frac{2(W_{rv1} - W_{rv2})}{h_{rv1}} \cdot \frac{1}{Ln(\frac{W_{rv1}}{W_{rv2}})} \tag{15}$$

$$P_{rv2} = \mu_c L_{stk} \frac{2h_{rv2}}{W_{rv2} + W_{rv3}} \tag{16}$$

$$P_{rv2} = \mu_c L_{stk} \frac{2h_{rv3}}{W_{rv3} + W_{rv4}} \tag{17}$$

$$P_{rv4} = \mu_c L_{stk} \frac{2(W_{rv5} - W_{rv4})}{h_{rv4}} \cdot \frac{1}{Ln(\frac{W_{rv5}}{W_{rv4}})} \tag{18}$$

Due to complex routes of flux lines in the area between the two sides of a V-shaped arrangement with $\beta$ angle, a mesh network with a sector of circle shape is considered in the proposed EMN model. The relations of permeances in this network with $M_r$-rows and $N_r$-columns are as follows:
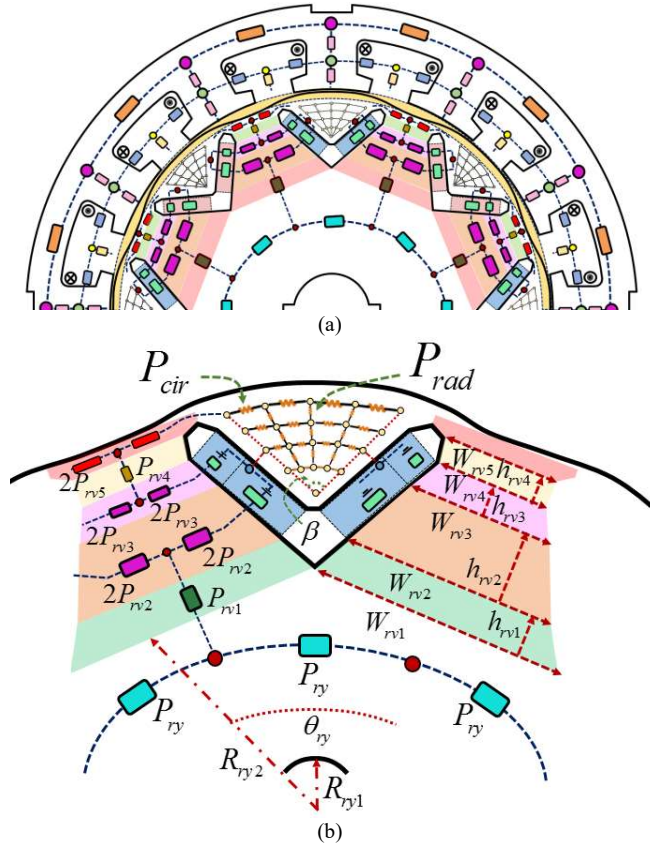


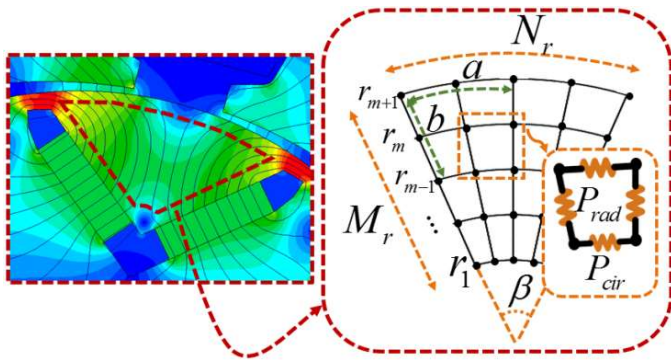Fig. 9. (a) Schematic view of stator and rotor EMN models, (b) constant rotor permeances.

Fig. 10. Reluctance network modelling triangular-shaped area between two sides of V-shaped PM housing.

$$M_r = \frac{r_{m+1} - r_1}{b/2} \quad , \quad N_r = \frac{r_{m+1}}{a/2}\beta \;\rightarrow\; \frac{N_r}{M_r} = \frac{b}{a}\beta\frac{1}{1 - \frac{r_1}{r_{m+1}}} \tag{19}$$

The radial and peripheral permeances, $P_{rad}$ and $P_{cir}$, shown in a mesh cell of Fig. 10, can be calculated as follows:

$$P_{rad} = \mu_c L_{stk}\frac{2\beta}{N_r}\cdot\frac{1}{Ln(\frac{r_{m+1}}{r_m})} \tag{20}$$

$$P_{cir} = \mu_c L_{stk}\frac{\beta}{N_r}\cdot Ln(\frac{r_{m+1}}{r_{m-1}}) \tag{21}$$

In the model, the $N_r$, $M_r$ and $\beta$ are selected 4, 3 and $5\pi/9$, respectively. Table II lists the dimensional variables of $M_1$ design of the proposed VR-FS-VPM machine, used in (4)-(12).

TABLE II
DIMENSIONS OF STATOR AND ROTOR (in mm)

| $R_{sy1}$ | 53.5 | $\theta_{sy}$ | 30 | $h_{PM}$ | 3 | $h_{rv1}$ | 3.5 |
|---|---|---|---|---|---|---|---|
| $R_{sy2}$ | 60 | $W_{rv1}$ | 21.5 | $h_s$ | 5 | $h_{rv2}$ | 6.5 |
| $R_{ry1}$ | 7.5 | $W_{rv2}$ | 18.5 | $W_s$ | 16 | $h_{rv3}$ | 3.5 |
| $R_{ry2}$ | 25 | $W_{rv3}$ | 12.5 | $W_{so}$ | 8 | $h_{rv4}$ | 1.5 |
| $l_{stk}$ | 25 | $W_{rv4}$ | 9.2 | $W_{PM}$ | 10 | $h_{rv5}$ | 1.5 |
| $\theta_{ry}$ | 45° | $W_{rv5}$ | 10 | $h_w$ | 2.5 | $h_{so}$ | 2.5 |
| $W_t$ | 10 | a | 2.5 | b | 2.5 | $\beta$ | 100° |

### C. Air gap Network with Pentagonal Mesh Design

According to Fig. 11, the design of floret pentagonal tiling (FPT) is inspired for shaping the mesh network of air gap region. In this way, the accuracy of evaluated flux density distributions in the radial and tangential directions is enhanced and cogging torque is reduced. The magnetic permeances considered for modeling flux tubes should allow complex pattern of flux lines to be created especially lines passing the tooth tips and slot opening boundaries. This cannot be achieved using only horizontal or vertical mesh cells. A high resolution mesh density is needed to achieve an acceptable accuracy using quadrilateral and triangular shapes of mesh cells. Hence, the number of mesh layers and the computation burden increase, which is undesirable. To accurately capture the irregular and complex flux routes in the air gap region with reasonable solution time, pentagonal shape mesh cell is used to model the air gap region. A separate area is considered for calculation of each permeance without overlapping with the
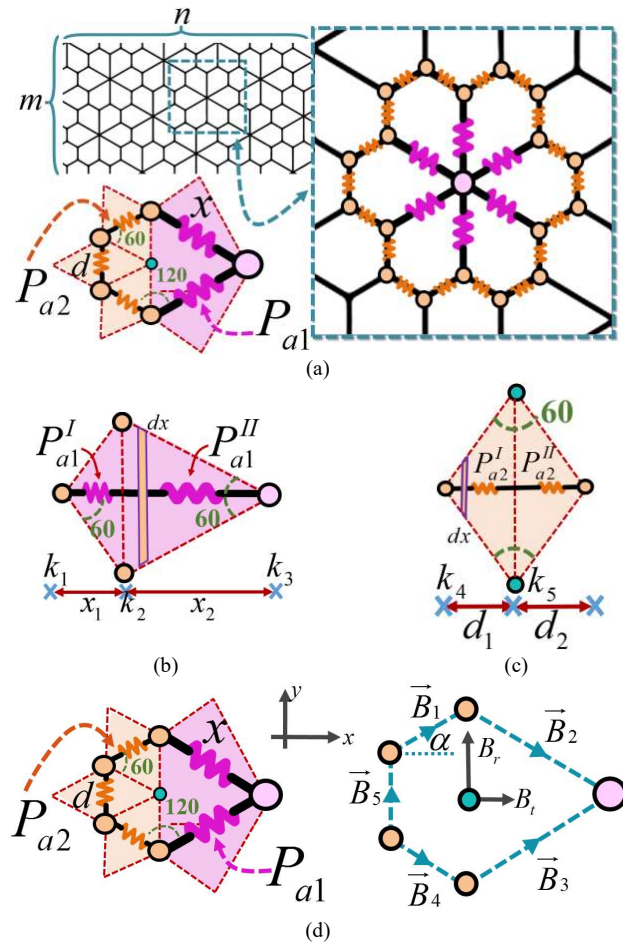


Fig. 11. Pentagonal-shaped mesh cell for air gap permeance network, (a) view of meshing, (b) $P_{a1}$ calculation, (c) $P_{a2}$ calculation, and (d) a magnetic flux density vector for each mesh cell side.

other areas to achieve the most accessible level of accuracy. Three sides of a pentagonal mesh cell have $x$ length and two of them have $d$ length. In this cell shape, one of the created angles is $60^0$ and the others are $120^0$. Permeance $P_{a1}$ consists of two series permeances $P^I_{a1}$ and $P^{II}_{a1}$, i.e. $P_{a1} = P^I_{a1} + P^{II}_{a1}$. $P_{a2}$ is created from the series connection of two equal permeances of $P^I_{a2}$ and $P^{II}_{a2}$.

To get the same values independent of the mesh cell dimensions, all the air gap network permeances are calculated using the method presented in [17]. In other words, the integration bounds of $k_1$, $k_2$ and $k_3$ are selected to have equal permeances of pentagonal mesh sides. All air gap network permeances are $\mu_0 L_{stk}$. The air gap network permeances are as follows:

$$P^I_{a1} = \mu_o L_{stk}\frac{1}{\int_{k1}^{k2}\frac{1}{2\sqrt{3}x'}dx'} = \frac{2\sqrt{3}\mu_o L_{stk}}{Ln(\frac{k_2}{k_1})} \tag{22}$$

$$P^{II}_{a1} = \mu_o L_{stk}\frac{1}{\int_{k2}^{k3}\frac{1}{\frac{\sqrt{3}}{3}(x-x')}dx'} = \frac{\mu_o L_{stk}}{\sqrt{3}Ln(\frac{x-k_2}{x-k_3})} \tag{23}$$

This article has been accepted for publication in IEEE Transactions on Transportation Electrification. This is the author's version which has not been fully edited and content may change prior to final publication. Citation information: DOI 10.1109/TTE.2023.3235333

9

$$P_{a2}^{I} = P_{a2}^{II} = \mu_o L_{stk} \frac{1}{\int_{k4}^{k5} \frac{1}{2\sqrt{3}x'}dx'} = \frac{2\sqrt{3}\mu_o L_{stk}}{Ln(\frac{k_5}{k_4})} \qquad (24)$$

As shown in Fig. 11(c), $k_5/k_4$ ratio is the same as $k_2/k_1$ ratio. To obtain the same value, i.e. $\mu_0 L_{stk}$, for all permeances, the relations between dimensional values of a mesh cell are determined as follows:

$$P_{a1}^{I} = P_{a2}^{I} = 2\mu_o L_{stk}$$

$$\rightarrow Ln\frac{k_5}{k_4} = Ln\frac{k_2}{k_1} = \sqrt{3} \rightarrow \begin{cases} k_5 = e^{\sqrt{3}}k_4 \\ k_2 = e^{\sqrt{3}}k_1 \end{cases} \qquad (25)$$

$$P_{a1}^{II} = 2\mu_o L_{stk} \quad \rightarrow \quad \frac{x-k_2}{x-k_3} = e^{\frac{1}{2\sqrt{3}}} \qquad (26)$$

$$\begin{cases} \frac{x_1}{x_2} = \frac{\tan(30°)}{\tan(60°)} = \frac{1}{3} \\ x_1 + x_2 = x \end{cases} \rightarrow x_1 = \frac{x}{4} \quad , \quad x_2 = \frac{3x}{4} \qquad (27)$$

$$\begin{cases} \frac{d_1}{d_2} = \frac{\tan(60°)}{\tan(60°)} = 1 \\ d_1 + d_2 = d \end{cases} \rightarrow d_1 = \frac{d}{2} \quad , \quad d_2 = \frac{d}{2}$$

A magnetic flux density vector is obtained for each mesh cell side. The vector for the central point of a pentagonal mesh in the air gap region is divided into normal and tangential components, $B_n$ and $B_t$, respectively. These components are obtained from the calculated magnetic field of the pentagonal mesh sides, using the following equations:

$$\overrightarrow{B_i} = \left\{ \overrightarrow{B_1}, \overrightarrow{B_2}, \overrightarrow{B_3}, \overrightarrow{B_4}, \overrightarrow{B_5} \right\}$$

$$\overrightarrow{B_{ag}^{cell}}(\theta,\varphi,\alpha) =$$

$$B_r^{cell}(\theta,\varphi,\alpha).\overrightarrow{a_r} + B_t^{cell}(\theta,\varphi,\alpha).\overrightarrow{a_t} = \sum_{i=1}^{5}\overrightarrow{B_i}(\theta,\varphi,\alpha) \qquad (28)$$

$$B_r = \frac{1}{2}\{B_1\sin(\alpha) - B_2\cos(2\alpha) + B_3\cos(2\alpha)$$
$$- B_4\sin(\alpha) + B_5\} \qquad (29)$$

$$B_t = \frac{1}{2}\{B_1\cos(\alpha) + B_2\sin(2\alpha) + B_3\sin(2\alpha) + B_4\cos(\alpha)\}$$

Since each magnetic field vector belongs to a common side of two adjacent pentagonal mesh cells, coefficient ½ should be considered above.

### D. Air gap Network with Quadrilateral Mesh Design

To fairly evaluate the effectiveness of the proposed pentagonal meshing method, the results of EMN model using this mesh structure for air gap region should be compared with the other common types of meshing designs. In this way, the air gap permeance network are modeled using the quadrilateral mesh design (QMD) as depicted in Fig. 12. In these mesh arrangements, a separate area without overlap is considered in the calculation of each permeance to model the air gap flux paths correctly. Fig. 12 shows the permeances of QMD mesh networks, $P_d$, consisting of two identical series
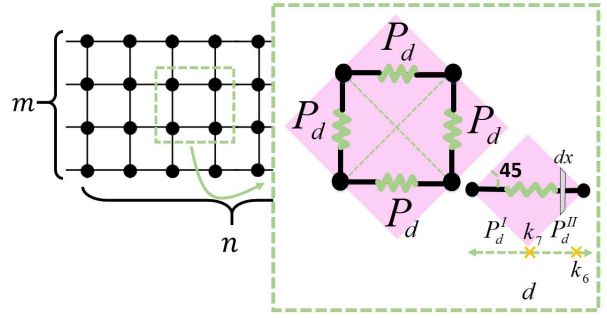


Fig. 12. Quadrilateral mesh cells for air gap region.

permeances as follows:

$$P_d = \frac{P_d^{I}.P_d^{II}}{P_d^{I} + P_d^{II}} = \frac{1}{2}\mu_o l_{stk} \frac{1}{\int_{k6}^{k7}\frac{1}{2\tan(45°).x}dx} = \mu_o l_{stk} \qquad (30)$$

where $k_7$=d/2. The air gap network permeances are considered $\mu_0 L_{stk}$ to eliminate the dependency between the permeance and mesh cell dimensions. Therefore, $k_7/k_6$ ratio is equal to $e$.

## IV. CALCULATION OF VARIABLE PERMEANCE CONNECTING ROTOR AND AIR GAP MESH NETWORKS

Variable air gap length of $M_1$ design leads to much complicated mesh based modeling. The mathematical mapping method can be effectively used for converting a complex geometry into a simpler one. Fig. 13 shows the conformal mapping. One type of mapping in which the scalar magnetic potential does not change is conformal mapping, where the local angles of the original and modified shapes are the same. This mapping is a powerful tool for analyzing different 2D fields, including magneto-static, electro-static, electro-dynamic and thermal fields. It is an analytical complex function that maps the original structure into a simpler geometry for solving the fields. The most important issue is to define the mapping function appropriately. This depends on the geometry of the solution domain. Suppose the closed $D$-region, i.e. the boundary of rotor outer surface, is a Jordan curve named J in the Z-complex plane, which is transformed to $D'$-region in W plane using W=f (z) mapping function with the constraints of f (0) =0 and f' (0)>0.

According to Osgood-Carathéodory theory [18], the complex function f can be mapped as a homeomorphism from the region $\bar{D}$ to $\bar{D}'$. As a result, there is a non-zero analytic function in region $\bar{D}$ and continuously in region D called s (z):

$$s(z) = Ln(\frac{f(z)}{z}) = u + jv \qquad (31)$$

where, $u$ and $v$ are the real and the harmonic functions in region $D$ and continuously in region $\bar{D}$ respectively. So, we can write:

$$s(z) \approx \sum_{k=-N}^{N} c_k.z^k \quad , \quad c_k = a_k + jb_k \qquad (32)$$

The $f$ mapping function can be defined as follows;

$$\Delta u = 0 \ , \ u = -Ln|z| \quad (z \in J) \ , \ v(0) = 0 \qquad (33)$$
$$\rightarrow \qquad f(z) = \alpha.ze^{u+jv}$$
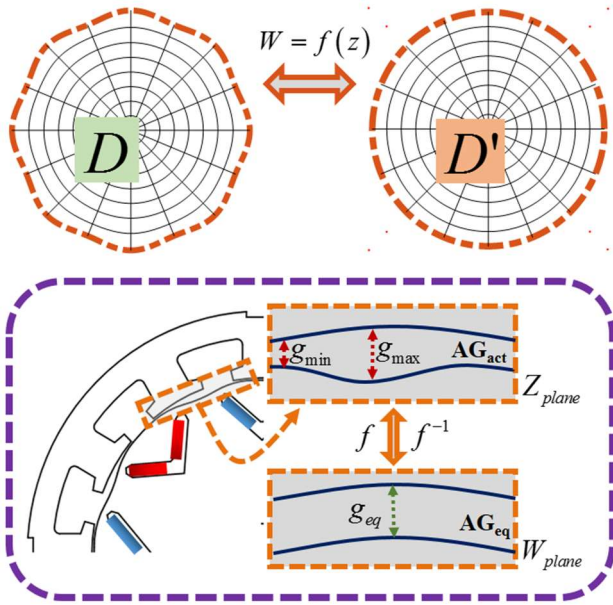
Fig. 13. Schematic of numerical conformal mapping.

$$u(z) \approx \mathrm{Re}(\sum_{k=-N}^{N} c_k . z^k) = \sum_{k=-N}^{N} (a_k . \mathrm{Re}(z^k) - b_k . \mathrm{Im}(z^k))$$

$$v(z) \approx \mathrm{Im}(\sum_{k=-N}^{N} c_k . z^k) = \sum_{k=-N}^{N} (a_k . \mathrm{Im}(z^k) + b_k . \mathrm{Re}(z^k))$$
(34)

If J-curve is a one-to-one function in Z-plane and this function and all of its derivatives are continuous, the mapping function s(z) can be estimated using a power series as (31). According to the solving algorithm of numerical conformal mapping, first $N$ should be selected to reach a reasonable accuracy. Then, parameter $u$ is obtained by getting $m$ sample points from the J-curve as such that $m>>N$. In the next step, coefficients $a_k$ and $b_k$ are estimated using Arnoldi-factorization method [19] by solving least square problem in the form of A.x=B and considering the stability challenge.

In the next step, the relations of magnetic permeances mapped to W-plane should be derived. The permeances are modeled as differential elements in Z- and W-planes as shown in Fig. 14, their relations are as follows:

$$dP_z = \mu_c dL_{stk} \frac{\partial n_z}{\partial t_z} \quad , \quad dP_w = \mu_c dL_{stk} \frac{\partial n_w}{\partial t_w}$$
(35)

$$dP_w = \mu_c dL_{stk} \frac{\partial n_w}{\partial t_w} = \mu_c dL_{stk} \frac{\partial f(n_z)}{\partial f(t_z)} \times \frac{\partial n_z}{\partial t_z} \times \frac{\partial t_z}{\partial n_z}$$
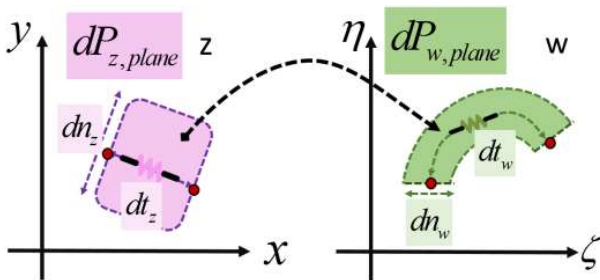(36)



Fig. 14. Modeled permeances as differential elements in Z- and W-planes.

Therefore, the relation between the mapped and the original permeance is as follows:

$$\frac{dP_w}{dP_z} = \frac{\partial f(n_z)}{\partial n_z} \times \frac{\partial t_z}{\partial f(t_z)} \rightarrow$$

$$P_w = \int \frac{\partial f(n_z)}{\partial n_z} \times \frac{\partial t_z}{\partial f(t_z)} dP_z$$
(37)

The air gap and rotor Maxwell equations for both complex original geometry and the simplified circular mapped geometry can be written as follows:

$$
\begin{aligned}
&in \ air-gap \ region: \\
&\nabla \times B_z = 0 \quad , \quad \nabla.B_z = 0 \quad \rightarrow \quad B_z = -\nabla \varphi_z = -\nabla \times A_z \\
&\nabla \times B_w = 0 \quad , \quad \nabla.B_w = 0 \quad \rightarrow \quad B_w = -\nabla \varphi_w = -\nabla \times A_w \\
&in \ rotor \ region: \\
&\nabla \times B_z \neq 0 \quad , \quad \nabla.B_z = 0 \quad \rightarrow \quad B_z = -\nabla \times A_z \\
&\nabla \times B_w \neq 0 \quad , \quad \nabla.B_w = 0 \quad \rightarrow \quad B_w = -\nabla \times A_w
\end{aligned}
$$
(38)

According to conformal mapping theorem, scalar and vector magnetic potentials are the same for original and mapped areas.

$$\varphi_z = \varphi_w \quad , \quad A_w = A_z$$
(39)

The W-plane flux density from the Z-plane is evaluated as follows:

$$B_w = \frac{B_z}{(\frac{\partial w}{\partial z})^*}$$
(40)

The next step is defining and calculating the variable permeances between the mapped rotor geometry and the air gap as a function of the rotor position. Now, the air gap region is a disk-shape area and the sides of the pentagonal mesh cells can be accommodated in $m$ rows and $n$ columns as shown in Fig. 15(a). Each air gap permeance in the air gap inner layer of mesh network covers $\theta_{n,ag}=360^o/n_{air \ gap,Node}$ angle, where, $n_{air \ gap,Node}$ is the number of nodes in innermost layer of the air gap mesh network which is obtained as follows:

$$\frac{n_{air-gap,Node}}{m_{air-gap,Node}} = \frac{\pi D_{ave}}{g_o - l_b}$$
(41)

On the other hand, there are $N_r$ nodes on the outermost layer of mesh network of the rotor core covering angle of $\theta_{rt}= 360°/N_r$ for each node. $N_r$, obtained from (19), is lower than $n_{air \ gap,\text{Node}}$, hence, $\theta_{rt}>\theta_{n,ag}$. Each $N_r$ node is connected to $N_{vp}$ varying permeances. These permeances are connected to the air gap permeances according to the defined continuous positioning algorithm.

Fig. 15(b) shows the connection of $i$-th node of the air gap innermost mesh layer and $j$-th node of rotor outermost mesh layer at two different time steps. The continuous positioning method (Fig. 15(c)) and its differences with the discrete positioning method (Fig. 15(d)) are discussed with full details in [17].
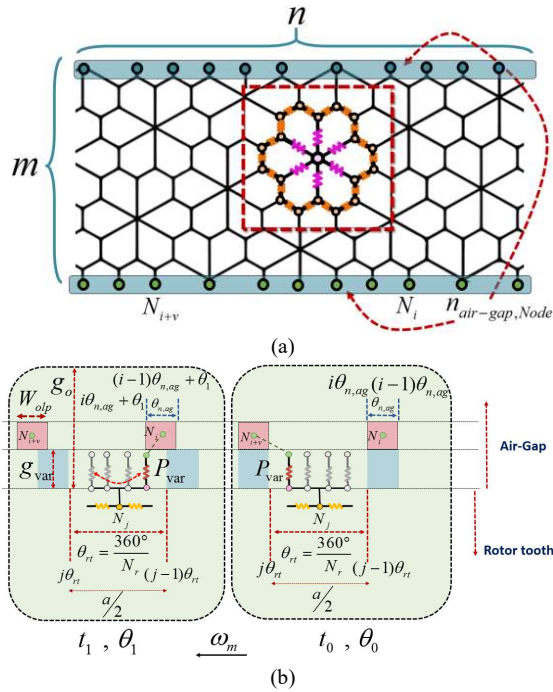
(a)



(b)

Fig. 15. (a) Positioning of variable permeance, (b) variable permeance and overlap areas.



Fig. 16: Flowchart for proposed EMN model.

## V. Flowchart of Proposed EMN-MODEL

The permeance network of the proposed geometry consists of 3115 nodes and 6336 branches. The resulted system of equations can be solved using Gaussian elimination method with partial pivoting. The non-linear magnetization characteristic can be applied to the Z-plane quantities for updating magnetic permeability. The completely analytical procedure and relations for mapped geometry in W-plane is the same as presented in [18]. Fig. 16 presents the flowchart of proposed solution method.

The flux density of branches in Z-plane ($B_{b,z}$) is obtained from its related values in W-plane ($B_{b,w}$) as follows:

$$B_{b,z} = B_{b,w} \cdot \left(\frac{\partial w}{\partial z}\right)^* \tag{42}$$

The magnetic permeability matrix can be evaluated from the magnetization characteristic of iron core and $B_{b,z}$. For core with homogenous magnetic properties, the magnetic permeability does not depend on the geometry parameters, hence, $\mu_w = \mu_z$.

## VI. FEA MODEL AND EXPERIMENTAL VERIFICATION

In this section, the proposed EMN model is validated by comparing its results with the FEA and the experimental results. For this purpose, the cogging torque, phase flux-linkage, back EMF, air gap flux density distribution and the loading characteristics waveforms are compared.

Fig. 17(a)-(c) shows the picture of the stator and rotor parts of the prototyped VR-FS-VPM motor. Fig. 17(d) exhibits the test-rig. The speed of the machines is controlled by a designed and fabricated power electronics drive. The magnetic core material is M470-50A and N42-SH grade of NdFeB magnet
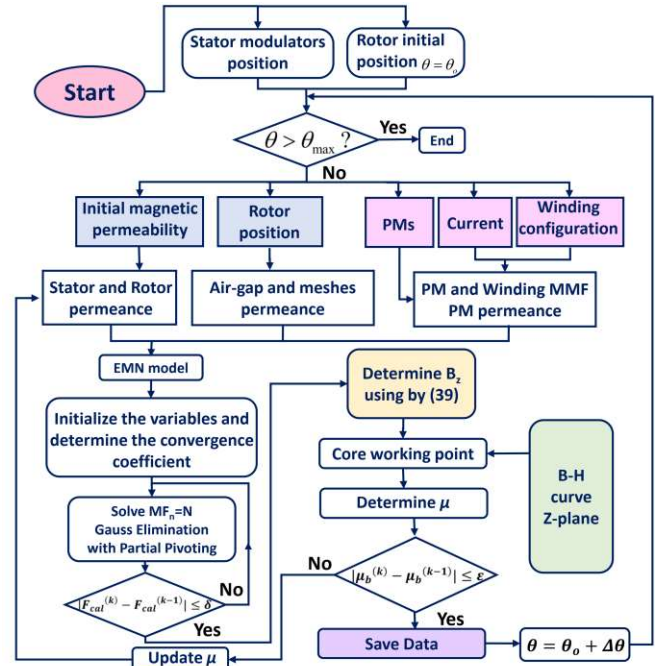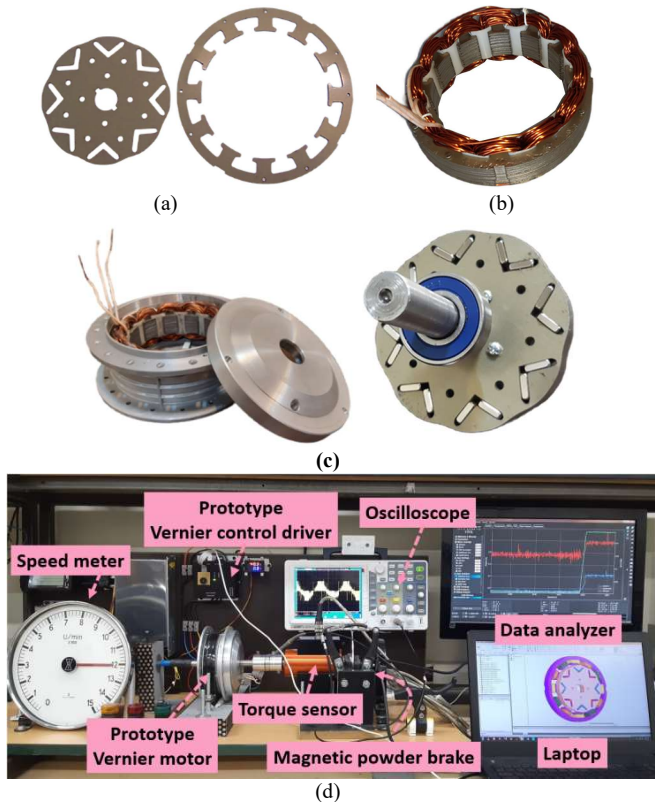


(a)                    (b)



(c)



(d)

Fig. 17. Experimental evaluation, (a) stator and rotor core sheet, (b) stator winding, (c) assembled rotor and stator, and (d) experimental test setup.

are used. Table III summaries the material types of different parts of the prototyped motor. Dr. Staiger Mohilo-0260 DM torque transducer was used for measuring developed torque and incremental encoder of Autonics with 8000 pulses per rotation was employed to measure the rotating speed. A controllable eddy current brake was connected to the motor as the mechanical load.

TABLE III
MATERIAL SPECIFICATION

| Part | Material type | Part | Material type |
|------|---------------|------|---------------|
| Stator & rotor | Lam. – M-470-50A | Flux barrier | Wood |
| PM | NdFeB – N42-SH | Housing | Aluminum 7000 |
| Rotor shaft | Mo-40 | Winding | Cu |

## A. Flux-linkage and EMF Waveforms

Fig. 18 compares the flux-linkage waveforms of $M_1$ and $M_2$ designs of proposed VR-FS-VPM machine with those obtained from FEA. Small differences between the results of the proposed EMN model and the FEA results are due to numerical errors. Fig. 19 shows the back-EMF for $M_1$ and $M_2$ designs, calculated from flux-linkage waveform, obtained from the proposed EMN model, and FEA.

## B. Air gap Flux Density Waveform

Fig. 20 compares the waveforms of the radial components of the air gap flux density obtained from the proposed EMN model of pentagonal mesh cell for air gap region with the FEA results. Another desirable feature of the proposed model is its ability to consider fringing and leakage flux components, as shown in Fig. 7, by appropriate design of air gap and slot-opening permeance network and placing $P_{vls}$, and $P_{hls}$ permeances (Fig. 8). The small difference between the peak amplitudes is related to the number of air gap mesh elements. Obviously, the accuracy may be further improved by increasing the mesh number at the cost of a longer computation time.

## C. Cogging Torque Waveform and Output Characteristics

The cogging torque reduction is eagerly pursued especially in the PM machines. A comprehensive procedure for analytical evaluation of cogging torque distribution in the EMN model with the pentagonal air gap meshing has been presented in [12, 17]. Fig. 21 illustrates the cogging torque variations obtained from FEA, EMN model and experiments. The small error is due to the simplification in calculation of air gap magnetic energy and considering only radial components of magnetic field of the mesh cells. The measured cogging torque was recorded using torque transducer at discrete positions displaced by 5 mechanical degrees. The friction of bearings is negligible, because of low speed and measuring steady-state torque. The peak-peak value of cogging torque is almost 0.07 Nm, or 1.7%.
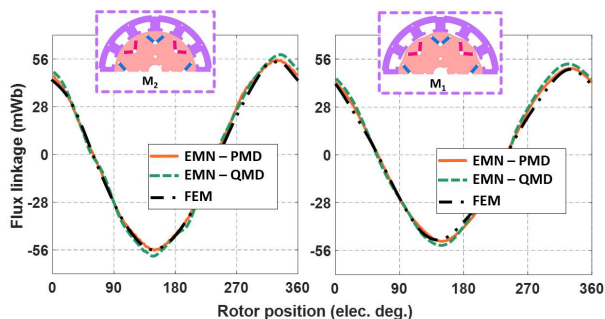


Fig. 18. Comparison of flux-linkage of EMN model, and FE model.
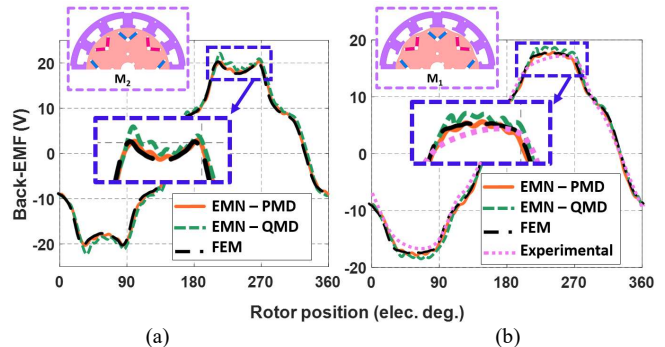


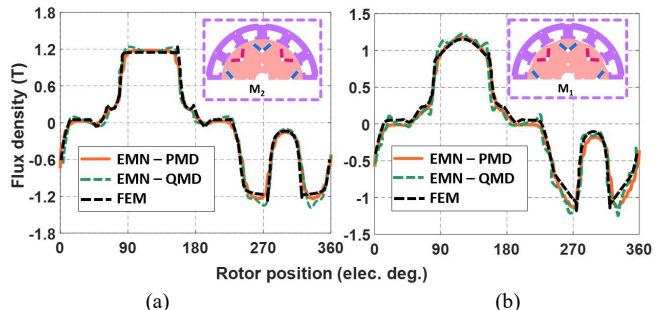Fig. 19. Comparison of line to line Back-EMF of EMN model and FE model.



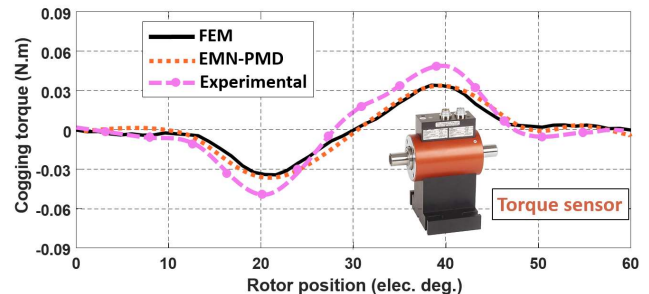Fig. 20. Comparison of flux density of EMN model and FE model.



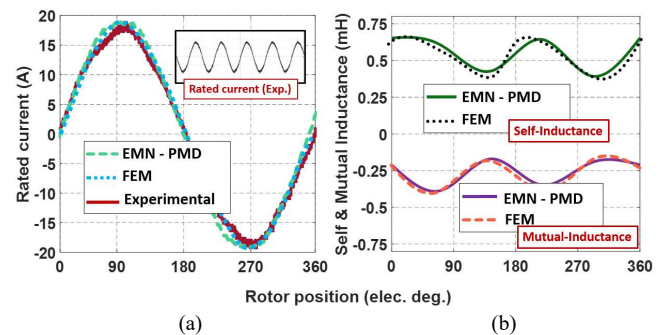Fig. 21. Comparison between cogging torque profiles using FEA, proposed EMN model and test.



Fig. 22. Result comparison (a) rated current and, (b) self and mutual inductance.

The analytically calculated self- and mutual-inductances curves are compared with those of FEA, which are well agree with small differences (Fig. 22(b)). Fig. 22(a) compares the winding current waveform under the rated operating conditions. Fig. 23 presents the developed electromagnetic torque at the rated load. Fig. 24 shows the torque-speed characteristic, the rated torque and the efficiency variations versus current phase angle. Due to limited operation of power electronics drive in flux-weakening region, the measurements
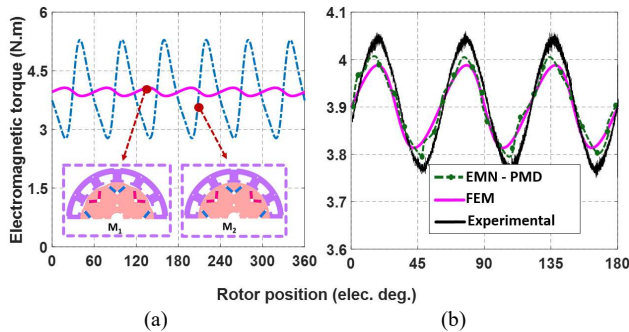
(a)                              (b)

Fig. 23. Comparison of electromagnetic torque.
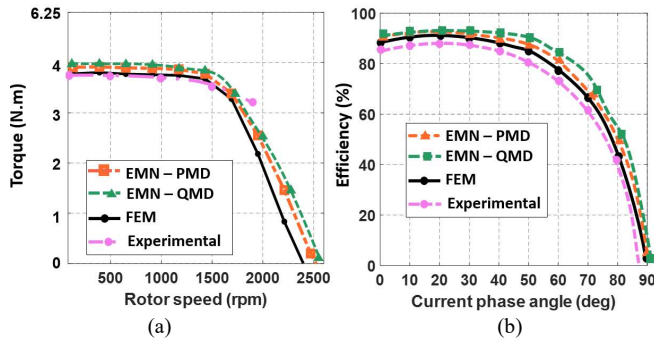


(a)                              (b)

Fig. 24. (a) Torque-speed curves. (b) efficiency-current phase angle curves.

are limited. It shows the accuracy of the proposed model and its validity over wide operating region from standstill up to high rotating speeds.

### D. Comparison of Numerical Performance

Table IV reports the elapsed times for running the proposed EMN with the pentagonal mesh design (EMN-PMD), an alternative EMN with the quadrilateral mesh design (EMN-QMD) and simulation using commercial FE software. It is noted that the mesh densities are chosen different to obtain almost the same accuracies.

TABLE IV
MESH DETAILS AND COMPUTATIONAL TIMES USING FEA AND PROPOSED METHOD

| Parameter | EMN - PMD | EMN - QMD | FEA |
|---|---|---|---|
| Number of mesh nodes | 3115 | 3276 | 205437 |
| Running time under Rated-load condition (s) | 1033 | 1245 | 6945 |
| Running time under no-load condition (s) | 947 | 1112 | 5213 |

### E. Unbalanced Magnetic Pull Characteristics

The reason for unbalanced magnetic pulls (UMPs) in PM machines is eccentricity or windings faults. The UMPs cause reduction of effective life span of the bearings, generating vibration and acoustic noise in electric machines. The fractional-slot SPM machines have very large effective air gap length due to PM permeability (nearly 1).Therefore, estimation of UMPs needs accurate knowledge 2D distribution of the air gap magnetic field . Eccentricity faults cause electromagnetic stress on the rotor of the machine. Radial direction of this stress is the same as UMP which leads to the displacement of the rotor from its symmetrical center. This will continues up to wearing rotor and stator. The x and y components of UMP can

be estimated using Maxwell electromagnetic stress method as follows:

$$\begin{cases} F_x^{UMF} = \dfrac{R_g l_{stk}}{2\mu_0} \displaystyle\int_0^{2\pi} (B_r^2 - B_\theta^2).\cos\varphi + 2B_\theta B_r.\sin\varphi d\varphi \\ F_y^{UMF} = \dfrac{R_g l_{stk}}{2\mu_0} \displaystyle\int_0^{2\pi} (B_r^2 - B_\theta^2).\sin\varphi - 2B_\theta B_r.\cos\varphi d\varphi \end{cases} \quad (43)$$

where

$$\begin{cases} B_\theta(\varphi,\theta) = B_{\theta.PM}(\varphi,\theta) + B_{\theta,Stator}(\varphi,\theta) \\ B_r(\varphi,\theta) = B_{r.PM}(\varphi,\theta) + B_{r,Stator}(\varphi,\theta) \end{cases} \quad (44)$$

Fig. 25 shows the x and y components of UMP at the rated load. Referring to the diagram and comparing modeling method and FEA, it is realized that the suggested method has a very good accuracy. The reason is the accuracy of the radial flux density modeling.
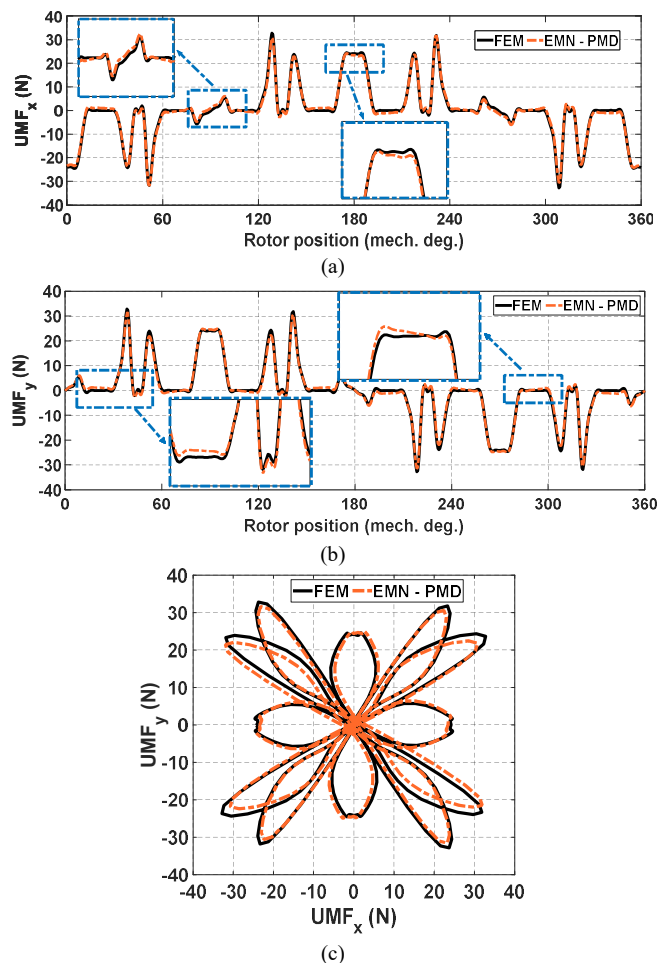


(a)



(b)



(c)

Fig. 25. The x and y components of UMP at the rated load along the air gap at a single rotor position.

### VII. CONCLUSION

This paper introduced an equivalent magnetic network (EMN) model for a VR-FS-VVPM machine with special rotor core structure which provides desirable accuracy and reasonable computational time ( maximum error lower than 10 %). The rotor surface was designed with variable reluctance to severely decrease the cogging torque, to lower than 2%, due to interaction between the PM field in the direct axis and the

stator teeth. A conformal mapping method was adopted for the non-linear solution algorithm to accurately predict the behavior of the flux lines in the air gap region of the VPM. Another contribution of the paper was defining the air gap permeance network using a special pentagonal-shaped mesh cell. Moreover, to reduce the leakage flux lines in the end-portion of PM segments and increase the torque density and power factor the special V-shaped housing was designed.

Finally, the effectiveness of the proposed structure applied to a prototyped 500 W, 12-slot/16-pole VR-FS-VVPM machine was confirmed by experiment. The validity and accuracy of the introduced analytical model were verified by comparing the results with the FEA and measured results. Studies in the design optimization of proposed V-shaped VPM machines can be progressed using the proposed EMN method to introduce it as a good option for using in EVs due to its promising features.

## REFERENCES

[1] X. Zhu, C. H. Lee, C. Chan, L. Xu, and W. Zhao. "Overview of flux-modulation machines based on flux-modulation principle: topology, theory, and development prospects", *IEEE Trans. on Transportation Electrification*, vol. 6, no. 2, pp. 612-624, 2020.

[2] M. Ghods, Z. Nasiri-Gheidari, F. Tootoonchian and H. Oraee, "Design improvement of a small, outer rotor, permanent magnet Vernier generator for supplying traffic enforcement camera," *IEEE Trans. on Energy Conversion*, vol. 33, no. 3, pp. 1213-1221, Sept. 2018.

[3] J. Faiz, M. Ghods, M.H. Arianborna, and M.A. Bazrafshan, "Single stator-single rotor permanent magnet Vernier machine topologies for direct-drive applications: Review and case study," *International Trans. on Electrical Energy Systems*, vol. 31, no. 12, 2021.

[4] H. Gorginpour, "Analysis and design considerations of an axial-flux dual-rotor consequent-pole Vernier-PM machine for direct-drive energy conversion systems", *IET Renewable Power Generation*, vol. 14, no. 2, pp. 211 – 221, 2020.

[5] F. Wu, and A. El-Refaie, "Permanent magnet Vernier machine: A review", *IET Electric Power Applications*, vol. 13, no. 2, pp. 127-137, 2018.

[6] Xu, L., Zhao, W., Wu, M., and Ji, J. "Investigation of slot–pole combination of dual-permanent-magnet-excited Vernier machines by using air gap field modulation theory", *IEEE Trans. on Transportation Electrification*, vol. 5, no. 4, pp. 1360-1369, 2019

[7] H. Gorginpour, "Dual-stator consequent-pole Vernier PM motor with improved power-factor", *IET Electric Power Application*, vol. 13, no. 5, pp. 652-661, 2019.

[8] Y. Chen, X. Zhu, L. Quan, Z. Xiang, Y. Du and X. Bu, "A V-shaped PM Vernier motor with enhanced flux-modulated effect and low torque ripple", *IEEE Trans. on Magnetics*, vol. 54, no. 11, pp. 1-4, Nov. 2018.

[9] H. Ahmad and J. S. Ro, "Analysis and design optimization of V-shaped permanent magnet Vernier motor for torque density improvement," *IEEE Access*, vol. 9, pp. 13542-13552, 2021.

[10] W. Ren, Q. Xu and Q. Li, "Asymmetrical V-shape rotor configuration of an interior permanent magnet machine for improving torque characteristics", *IEEE Trans. on Magnetics*, vol. 51, no. 11, pp. 1-4, Nov. 2015.

[11] M. Ghods., J. Faiz, M.A. Bazrafshan, and M.H. Arianborna, "A mesh design technique for double stator linear PM Vernier machine based on equivalent magnetic network modeling," *IEEE Trans. on Energy Conversion*, vol. 37, no. 2, pp. 1087-1095, June 2022.

[12] B. Sheikh-Ghalavand, S. Vaez-Zadeh, and A. Hasanpour Isfahani, "An improved magnetic equivalent circuit model for iron-core linear permanent-magnet synchronous motors, " *IEEE Trans. on Magnetic.*, vol. 46, no. 1, pp. 112-119, 2010.

[13] M. Amrhein, and P. T. Krein, "3-D magnetic equivalent circuit framework for modelling electromechanical devices," *IEEE Trans. on Energy Conversion*, vol. 24, no. 2, pp. 397-405, 2009.

[14] J. Wang and J. Zhu, "A simple method for performance prediction of permanent magnet eddy current couplings using a new magnetic equivalent circuit model, "*IEEE Trans. on Industrial Electronics*, vol. 65, no. 3, pp. 2487-2495, 2018.

[15] S. Xiaodong, et al., "Real-time HIL emulation for a segmented-rotor switched reluctance motor using a new magnetic equivalent circuit, " *IEEE Trans. on Power Electronics*, vol. 35, no. 4, pp. 3841-3849, 2020.

[17] G. Liu, S. Jiang, W. Zhao, and Q. Chen, "Modular reluctance network simulation f a linear permanent-magnet Vernier machine using new mesh generation methods, " *IEEE Trans. on Industrial Electronics*, vol. 64, no. 7, pp. 23-32, July 2017.

[18] M. Ghods, H. Gorginpour, M. A. Bazrafshan and M. S. Toulabi, "Equivalent magnetic network modeling of dual-winding outer-rotor Vernier permanent magnet machine considering pentagonal meshing in the air gap", *IEEE Trans. on Industrial Electronics*, in-press.

[19] M. S. Mirazimi, and A. Kiyoumarsi, "Magnetic field analysis of SynRel and PMASynRel machines with hyperbolic flux barriers using conformal mapping", *IEEE Trans. on Transportation Electrification*, vol. 6, no. 1, pp.52-61, 2019.